JOURNAL OF MATERIALS SCIENCE 37 (2002) 2685–2691

An experimental study on the melt spinning of AA2618 alloy

W. LUO, M. YAN, W. Z. ZHU
National Key Lab of Silicon Material, Zhejiang University, Hangzhou 310027, People's Republic of China
E-mail: mse_yanmi@dial.zju.edu.cn

B. CANTOR
Department of Materials, University of Oxford, Parks Road, Oxford OX1 3PH, UK

The commercial AA2618 alloy was treated through melt spinning at rotation speeds of 20 and 40 ms^{-1}, respectively. The melt-spun ribbons were characterised by a combination of optical microscopy (OPM), scanning electron microscopy (SEM), transmission electron microscopy (TEM) and X-ray diffraction (XRD). Microstructural evolution of ribbons in the continuous heating process was investigated. Microhardnesses of samples treated under different conditions were measured. It was found that due to the low solubilities of iron and nickel Al_xFeNi was very prone to precipitate in AA2618 alloy. At chilling sides of melt-spun ribbons fine Al_xFeNi particles presented along the grain boundaries, while at free sides Al_xFeNi presented not only along the grain boundaries but also in the interior of grains. The microhardnesses of melt-spun ribbons decreased significantly from chilling surfaces to free surfaces. During heating Al_xFeNi precipitated uniformly throughout the matrix until melting, which was one of the reasons responsible for the lowering of hardness.

1. Introduction

There have been extensive researches on the precipitation and ageing hardening of Al-Cu-Mg alloy family [1–3]. Copper and magnesium were found to contribute to the precipitation hardening at temperatures up to 200°C. Addition of iron and nickel into Al-Cu-Mg alloys was found to lead to satisfactory mechanical properties at elevated temperatures up to 238°C [4, 5]. As a sort of Al-Cu-Mg-Fe-Ni alloy, AA2618 is primarily applied for production of pistons and aircraft engine components for operation at elevated temperatures [6, 7].

It is very interesting to know whether or not further addition of iron and nickel into Al-Cu-Mg alloys can lead to satisfactory performance of components when working at even higher temperatures. It has aroused the interest of some researchers [8]. The solution to the problem relies on better understanding of strengthening mechanisms of Al-Cu-Mg-Fe-Ni alloys under elevated temperatures. Formation of Al_xFeNi has been proved in the alloy under different processing conditions, and was found to play an important role in the strengthen of the alloys [6–9], although the structure of the aluminide has still not been recognized completely. The aluminide was determined by Zhang *et al*. [6, 8, 9] as Al_9FeNi, possessing a primitive monoclinic structure with lattice parameters of $a = 0.6213$ nm, $b = 0.6290$ nm, $c = 0.8557$ nm and $\beta = 94.76°$. In Oguocha *et al*.' work [7], however, the structural formula of different aluminide particles in cast AA2618 was found to be different, depending on the aluminum content in it. The aluminide was characterized as Al_xFeNi, having a C-centered monoclinic structure with lattice parameters $a = 0.8673$ nm, $b = 0.9000$ nm, $c = 0.8591$ nm, $\beta = 83.504°$. No matter what structure the aluminide possesses, Al_xFeNi presented significant effect on the mechanical performance of AA2618. In order to restrain the precipitation of Al_xFeNi, rapid solidification processing through melt spinning was applied to AA2618 alloy in this paper. The melt-spun microstructure and its evolution in the subsequent heating processing was investigated. The structure of Al_xFeNi is not within the scope of this investigation, since different processing routes and heat treatment history should be responsible for the difference in the reported aluminide structure.

2. Experimental details

The nominal composition of AA2618 is presented in Table I. Alloy strips, weighed about 5 g, were cut from the as-supplied commercial alloy, cleaned in methanol, and loaded in a quartz tube. The strips were remelted to 800°C in argon, then ejected from an orifice at the tube bottom to the rotating surface of a copper drum. The orifice diameter of quartz tube was 0.83 mm. The tangential rotation speed of the copper drum was 20 and 40 ms^{-1}, respectively.

The melt-spun ribbons were then subjected to microstructural characterization by a combination of

TABLE I The nominal composition of commercial AA2618 alloy

Cu (%)	Mg (%)	Fe (%)	Ni (%)	Si (%)	Ti (%)	Al (%)
2.3	1.6	1.1	1.0	0.18	0.07	Bal.

OPM, SEM, TEM, EDX and XRD. Philips 501 scanning electron mocroscope, and JEM 200CX analytical transmission electron microscope, both equipped with good quality modern energy-dispersive X-ray (LINK ISIS) systems, were used. XRD traces were obtained by using Philips PW 1729 diffractometer with filtered Cu Kα at a power of 5 kW. To observe different microstructural features across the ribbons, ribbons were polished either at the chilling surfaces (in contact with the copper drum), or at the free surfaces (in contact with the atmosphere) in the preparation of TEM foils, then further thinned by ion beam milling.

To investigate the evolution of Al_xFeNi morphology in the matrix, some pieces of ribbons were sealed in vacuumed silica tubes. The tubes were continuously heated to different temperatures, then quenched in water. After processing ribbons were taken out and subjected to microstructural characterization. A Dupont 2000 thermal analyzer was used to help examination of the precipitation behaviors of ribbons. DSC tests were carried out from 150°C to 750°C at a heating rate of 5 K/min under a dynamic argon atmosphere.

Measurements of microhardness were conducted at the transverse cross-sections of mounted ribbons, as a function of distance from the chilling surfaces. Microhardness was also measured on the chilling surfaces of ribbons quenched from different temperatures, as an indicator of effects of precipitated aluminide on the strength of alloy. For microhardness values obtained on chilling surfaces, each datum was the mean value of up to 50 points.

3. Results

3.1. The melt-spun structure of ribbons

The thicknesses of the ribbons were 50–70 μm and 40–50 μm, at the rotating speeds of 20 and 40 ms^{-1} respectively. Morphologies of both ribbons at the transverse cross-sections are presented respectively in Fig. 1a and b. It may be seen that there were featureless layers adjacent to chilling surfaces, and close to free surfaces the structure became coarser. This layered ribbon structure was expected, and has been reported in many investigations [10–12]. It has been established that the forming of featureless layers at chilling sides of ribbons is due to the homogeneous nucleation [10].

XRD profiles of the 20 and 40 ms^{-1} ribbons are given in Fig. 2 in comparison with that of untreated commercial AA2618 alloy. The profile of untreated alloy is labeled as A, and profiles of the 20 and 40 ms^{-1}

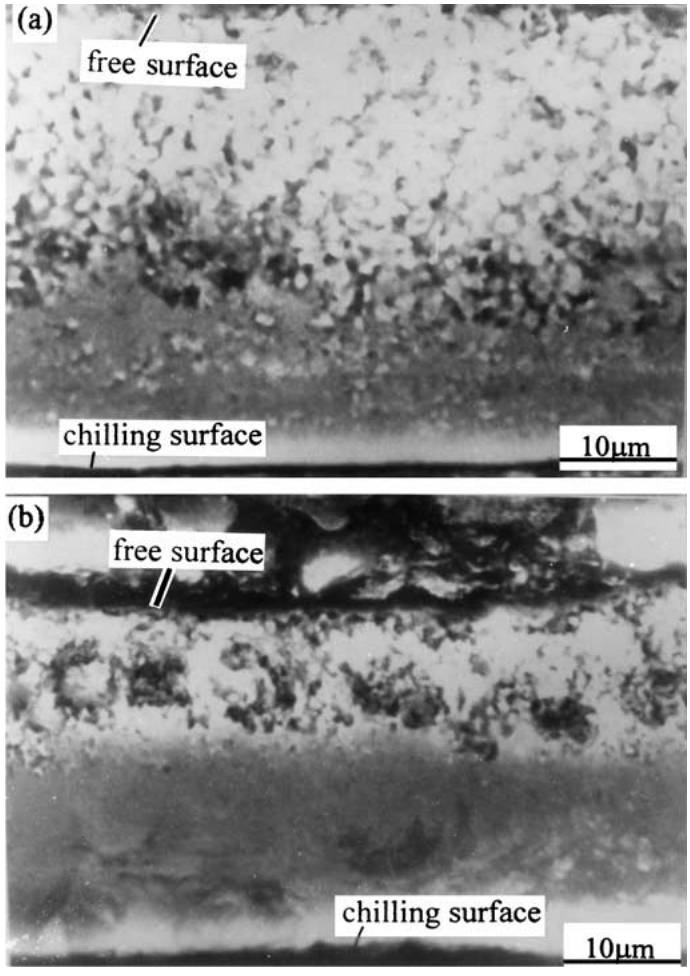

Figure 1 Morphologies of the ribbons at the transverse cross-sections: (a) at the rotation speed of 20 ms^{-1}, and (b) at the rotation speed of 40 ms^{-1}. Chilling surfaces are at the bottom of each micrograph.

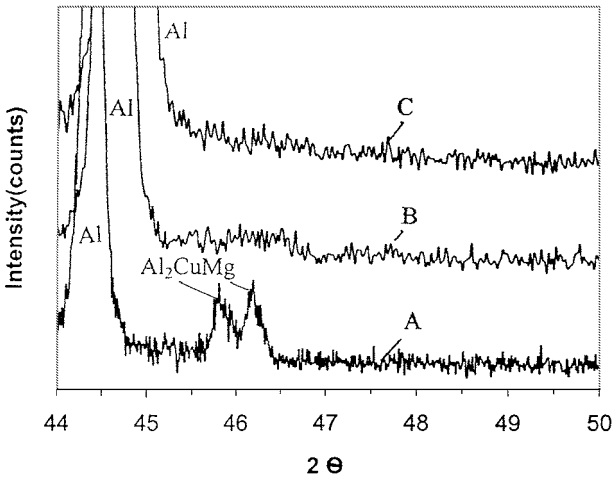

Figure 2 XRD profiles of ribbons in comparison with that of untreated AA2618 alloy: (A) the untreated alloy, (B) the 20 ms^{-1} ribbon, and (C) the 40 ms^{-1} ribbon.

ribbons were labeled as B and C, respectively. In all profiles there were no diffraction peaks which could be connected with Al_xFeNi. In profile A there were clear Al_2CuMg peaks. In profiles of both ribbons Al_2CuMg peaks disappeared, suggesting significant decreases of Al_2CuMg contents in ribbons, if any. The oversaturation of solute elements in matrix led to expansion of aluminum lattice, as evidenced by the shift of α-Al peaks in profiles B and C to larger 2θ values.

At chilling sides, the matrix of both 20 and 40 ms^{-1} ribbons was comprised of non-dendritic equiaxed grains, as demonstrated in Fig. 3a and b. The diameter of grains was typically 0.5 μm for the 20 ms^{-1} ribbon (Fig. 3a), and 0.4 μm for the 40 ms^{-1} ribbon (Fig. 3b). As can be seen in Fig. 3a, there were fine particles presented along the grain boundaries at the chilling side of the 20 ms^{-1} ribbon (Fig. 3a), the diameter of which was on the scale of tens of nanometres. Compared to the 20 ms^{-1} ribbon, the grain boundaries at the chilling side of the 40 ms^{-1} ribbon were relatively "clean". Precipitates were significantly fewer, but could still be found (Fig. 3b). At the chilling sides of both ribbons, no precipitates could be observed in the interior of grains.

Near the free sides, however, particles were observed to be separated out both in the interior of grains and at the grain boundaries. Moreover, grain boundaries were no longer straight (Fig. 3c and d), indicating that the growth of grains turned to be cellular.

EDX spectrum of the particles indicated that the precipitates were not Al_2CuMg, but Al_xFeNi. The spectrum was similar to the EDX spectrum of Al_xFeNi in AA2618 given by Oguocha *et al.* [7], indicating they were the same type of aluminide. A typical EDX spectrum of precipitates is presented in Fig. 4.

3.2. Microstructural evolution during heating

Microstructural observations for ribbons quenched from different heating temperatures indicated that Al_xFeNi precipitated and grew bigger steadily in the heating process. The higher the temperature reached, the larger the aluminide particles. While originally-presented Al_xFeNi particles grew bigger, new Al_xFeNi

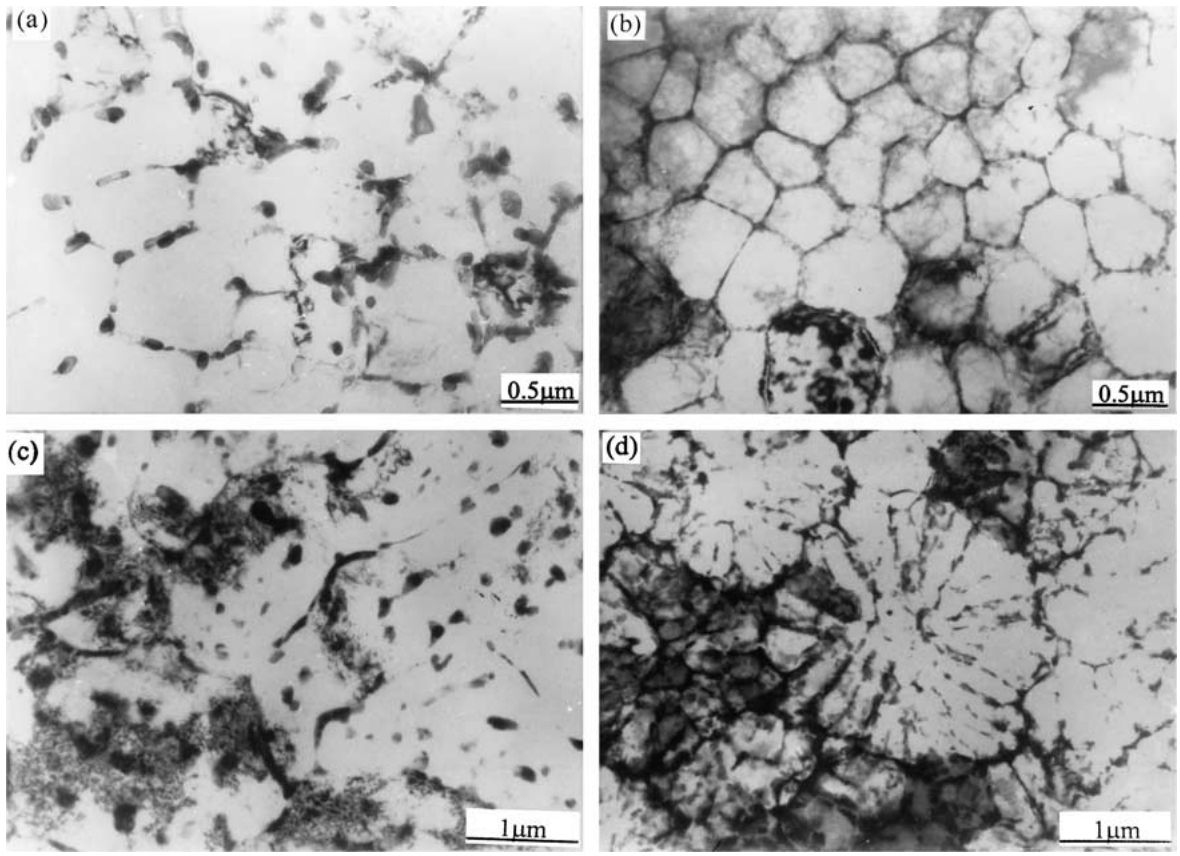

Figure 3 TEM observation at both sides of ribbons: (a) at the chilling side of 20 ms^{-1} ribbon; (b) at the chilling side of 40 ms^{-1} ribbon; (c) at the free side of 20 ms^{-1} ribbon; and (d) rosette-like grains at the free side of 40 ms^{-1} ribbon.

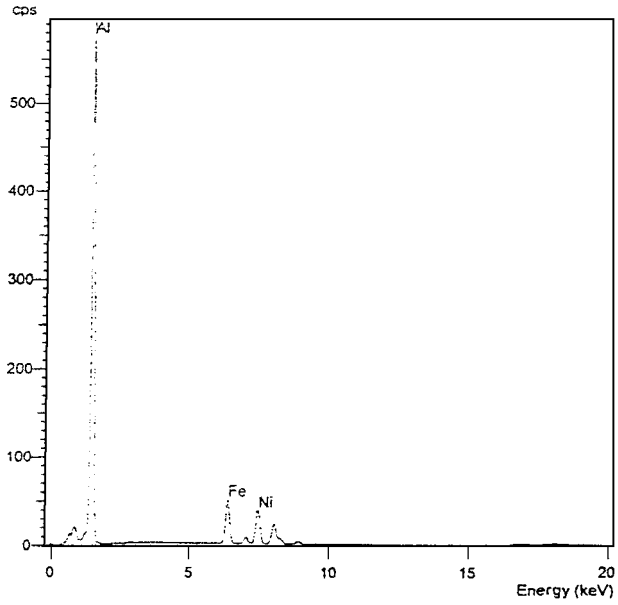

Figure 4 A typical EDX spectrum of the precipitates.

particles also precipitated. At the chilling sides of ribbons, Al_xFeNi was observed to be precipitated uniformly in the interior of grains where no precipitates presented originally. Morphologies of Al_xFeNi in the 20 ms^{-1} ribbon quenched from 80 and 520°C are shown in Fig. 5 and Fig. 6a and b, respectively. Heated to 80°C, the diameter of Al_xFeNi particles grew to over 100 nm. Heated to 520°C, the diameter of Al_xFeNi particles reached the order of 1 μm. Structures of the 40 ms^{-1} and 20 ms^{-1} ribbons were very similar. It was found that Al_xFeNi precipitated along the grain boundaries could impede the coarsening of aluminium grains. Grains were relatively smaller where more Al_xFeNi presented at the grain boundaries, and were relatively bigger where less Al_xFeNi presented at the grain boundaries.

DSC traces of 20 and 40 ms^{-1} ribbons, traces B and C, are illustrated in Fig. 7 in comparison with that of untreated alloy, trace A. Fig. 7 revealed that the aluminide could not dissolve in matrix on heating until melting with the surrounding Al-matrix. There were small endothermic peaks in traces of both ribbons, as labeled 1 and 2 in the figure. The onset temperature of the peaks was approximately 545.3°C. Combined with EDX microanalyses and microstructural observation of ribbons quenched from 553°C, peaks 1 and 2 can be attributed to the eutectic meltingof Al_xFeNi with the contacting aluminum. Since the content of Al_xFeNi was low in the untreated alloy, the peak of Al_xFeNi melting in trace A was not discernable.

3.3. Effect of precipitation on the microhardness

Since the ribbons were not very uniform, the local thicknesses of a ribbon were not the same along its length even in the same run. The local ribbon thickness affected the local hardness. Thus, microhardness values measured in different positions of the same ribbon could vary to some extents, according to the local thickness. A microhardness curve, which was measured at the transverse cross-section of the melt-spun 20 ms^{-1} ribbon, is illustrated in Fig. 8 against the spacing from the chilling surface. It can be seen that the microhardness decreased drastically from the chilling surface to the free surface, indicating that a higher cooling rate led to a higher hardness.

However, the microhardnesses of ribbons were not very higher compared with that of the untreated AA2618 alloy. Every datum in Fig. 9 was the mean values of around 50 measurements. As shown in the figure, the microhardness of untreated alloy was measured as HV 160.5. It was higher than the average microhardness measured on the chilling surface of the 20 ms^{-1} ribbon, HV152.3, but lower than the average microhardness measured on the chilling surface of the 40 ms^{-1} ribbon, HV 184.7. The microhardness of the 40 ms^{-1} ribbon was measured to be HV 146.4 when quenched from 200°C, HV119.14 when quenched from 535°C, and HV 107.52 when quenched from 553°C. It indicated that after heating the ribbon microhardnesses decreased steadily, which can attributed to the precipitation of alloying elements and coarsening of grains.

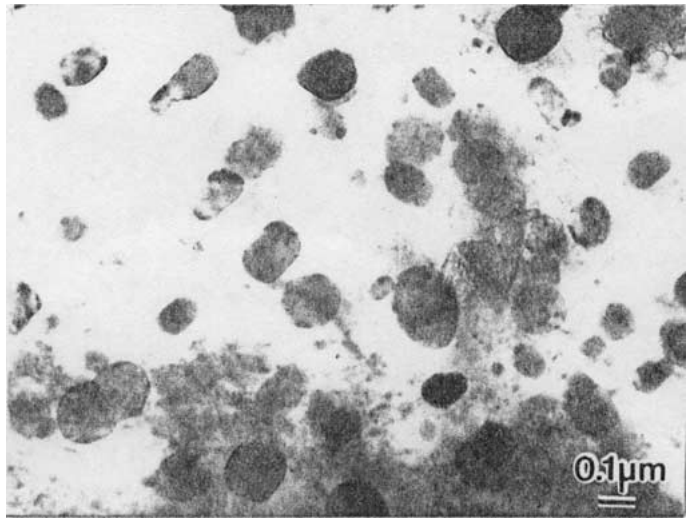

Figure 5 Morphology of Al_xFeNi in the 20 ms^{-1} ribbon quenched from 80°C (TEM).

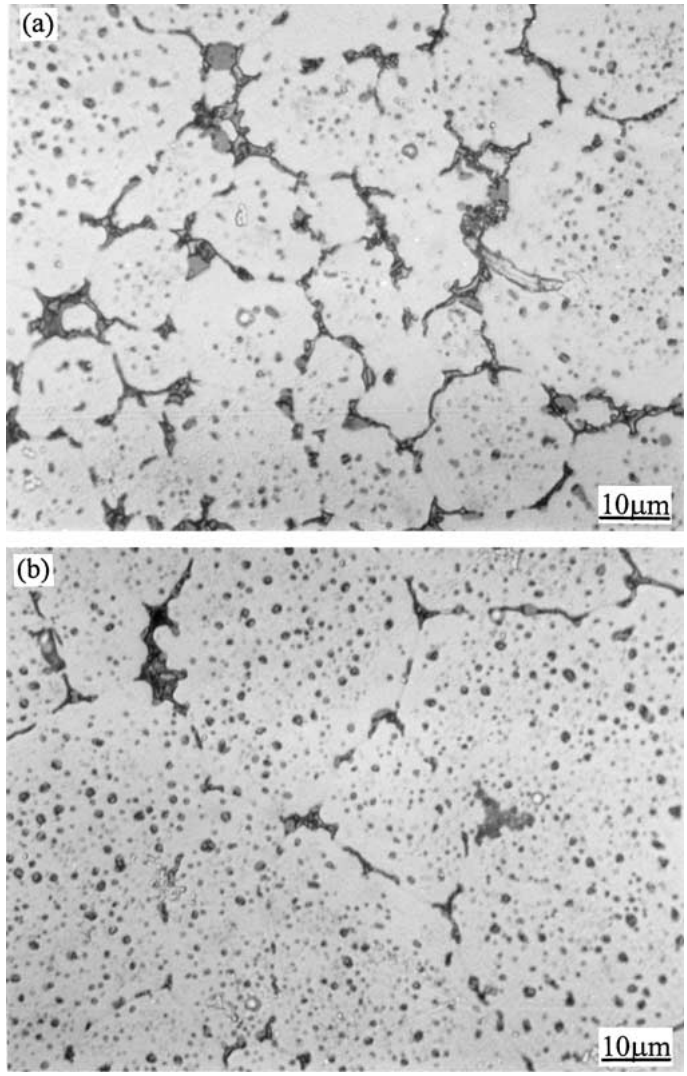

Figure 6 Morphology of Al_xFeNi in the 20 ms^{-1} ribbon quenched from 520°C (OPM). (a) grains were relatively smaller if more Al_xFeNi precipitated at the grain boundaries, and (b) grains were coarser if less Al_xFeNi precipitated at the grain boundaries.

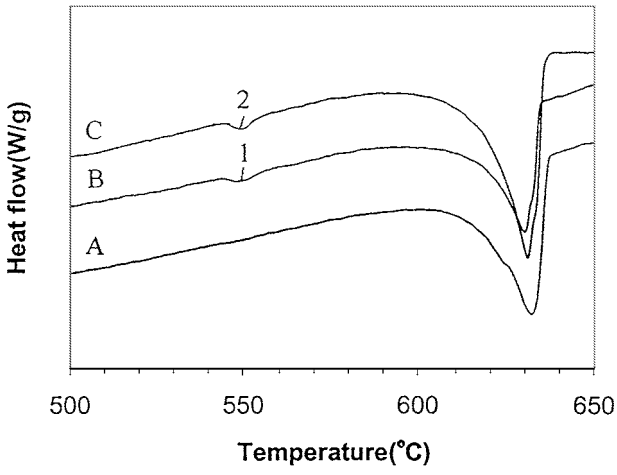

Figure 7 DSC traces of 20 and 40 ms^{-1} ribbons in comparison of that of untreated alloy: (A) the untreated AA2618, (B) the 20 ms^{-1} ribbon, and (C) the 40 ms^{-1} ribbon.

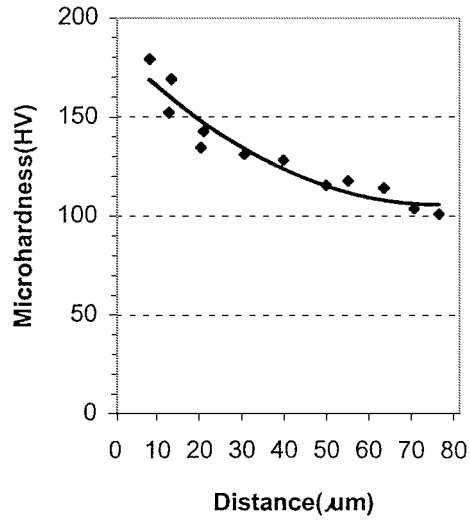

Figure 8 A curve of microhardness vs. the spacing from the chilling surface of the 20 ms^{-1} ribbon at the transverse cross-section.

4. Discussion

The cooling rates of melt spinning can be as high as 10^5–10^7 K/s [13]. Rapid solidification processing may lead to extended solubility, reduced segregation, grain refinement, and restraint of precipitation. However, at the chilling side of 40 ms^{-1} ribbon, where the cooling rate was the highest, there were still Al_xFeNi particles along the grain boundaries (seeing Fig. 3b). It indicated Al_xFeNi was very prone to precipitate.

From the Al-Fe and Al-Ni binary phase diagrams, it can be found that solubilities of iron and nickel in

TABLE II Solubility of elements in aluminium [14]

Temperature (°C)	Mg (%)	Cu (%)	Fe (%)	Ni (%)
300	3.2	0.5	≈0	≈0
100	1.0	0.1	≈0	≈0

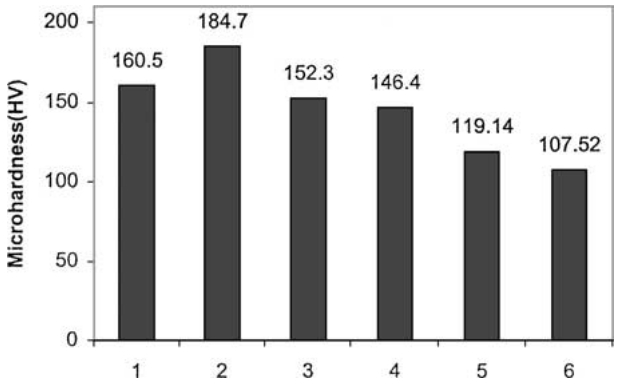

Figure 9 Comparison of microhardnesses obtained under different conditions. (1) On the untreated alloy, (2) on the chilling surface of the melt-spun 40 ms^{-1} ribbon, (3) on the chilling surface of the melt-spun 20 ms^{-1} ribbon, (4) on the 40 ms^{-1} ribbon heated to 200°C then quenched, (5) on the 40 ms^{-1} ribbon heated to 535°C then quenched, and (6) on the 40 ms^{-1} ribbon heated to 553°C then quenched.

aluminum at room temperature, or even at elevated temperatures were all close to zero, but solubilities of magnesium and copper were relatively high (seeing Table II). This explains why Al_2CuMg did not precipitate on melt spinning but Al_xFeNi precipitated. The cooling is approximately Newtonian over a small solidification temperature range, and the cooling rate is proportional to the rotating speed [13]. Thus, the local cooling rate at the chilling surface of the 20 ms^{-1} ribbon, was approximately half of that at the chilling surface of the 40 ms^{-1} ribbon, and solute microsegregation occurred to a higher extent compared with that at the chilling side of the 40 ms^{-1} ribbon. As a result, Al_xFeNi precipitates increased at the grain boundaries of the chilling side of the 20 ms^{-1} ribbon.

At chilling sides of both 40 and 20 ms^{-1} ribbons, the solidification rates were the highest, which led to the refined nondendritic structure. Away from the chilling surfaces, the grain size increased due to the decline of cooling rates. The relatively coarser structure observed at the free sides was formed through heterogeneous nucleation. The decrease of cooling rates resulted in the instability of solidification front, leading to the formation of cellular structure (Fig. 3c and d). When the cellular growth was radical, rosette or flower structure was formed (Fig. 3d) [14]. Moreover, due to the decrease of cooling rates the supersaturated matrix was less resistant to precipitation, and the coarsened grains made the distance for solute elements to diffuse to grain boundaries longer. As a result, at free sides Al_xFeNi precipitation also occurred in the interior of the grains, as shown in Fig. 3c.

Microhardness measurements of the melt-spun ribbons indicated that iron and nickel, when primarily dissolved in aluminum, could effectively strengthen the AA2618 alloy. Depending on the local cooling rates, the microhardness of supersaturated matrix could compare to, or even higher than the commercial AA2618 alloy which has been subjected to ageing treatment (Figs 8 and 9). The higher the cooling rate, the higher the ribbon microhardness. In addition to solution strengthening, grain refinement was also partly responsible for the high hardness of the melt-spun ribbons.

In the continuous heating process, the formation of GP zones and Al_2CuMg phase was restrained. Although they might form to some extent within the aging temperature range, the precipitation amount was limited since the period of time stayed in the range was short, and Al_2CuMg would dissolved rapidly when the temperature was above the range. Thus, the effect of aging on the hardness could be neglected. The variation of hardness primarily resulted from the precipitation of Al_xFeNi, superposed by the coarsening of aluminum grains. The result of microhardness measurements indicated that the massive precipitation led to the continuous decline of hardness; thus the steady precipitation of Al_xFeNi can lower the strength of AA2618 alloy at elevated temperatures. It suggested that further additions of iron and nickel in Al-Cu-Mg-Fe-Ni alloy might further strengthen the alloy to some extent, but the applications at high temperatures are still limited.

5. Conclusions

1. Al_xFeNi was prone to precipitate in the AA2618 alloy due to the low solubilities of iron and nickel. For AA2618 ribbons melt-spun at speeds of 20 and 40 ms^{-1}, refined Al_xFeNi particles could precipitate at the grain boundaries at chilling sides, and could precipitate both at the grain boundaries and in the interior of grains at free sides.

2. On continuous heating Al_xFeNi precipitated steadily. The starting melting temperature of Al_xFeNi with the surrounding Al-matrix was about 545.3°C.

3. The microhardnesses of melt-spun ribbons decreased significantly from chilling surfaces to free surfaces. The precipitation of Al_xFeNi was an important reason responsible for the lowering of hardness.

Acknowledgement

Some authors would like to thank the support of Special Research Foundation of High-Education Ph.D. Subjects, Education Ministry of China, and Foundation for Returned Overseas Chinese Students. Part of the work was carried out in laboratories of Department of Materials, University of Oxford, for which we are grateful.

References

1. S. L. CHEN, Y. ZHO, H. LIANG and Y. A. CHANG, *Metall. Mater. Trans.* A **28A** (1997) 435.
2. H. C. SHIH, N. J. HO and J. C. HUANG, *Metall. Mater. Trans.* **27A** (1996) 2479.
3. C. C. HUANG and S. W. CHEN, *Metall. Mater. Trans.* A **26A** (1995) 1007.
4. R. M. GOMES, T. SATO, H. TEZUKA and A. KAMIO, *Mater. Sci. Forum* **217–222** (1996) 789.
5. J. ZHOU, J. DUSZCZYK and B. M. KOREVAAR, *J. Mater. Sci.* **26** (1991) 824.

6. R. N. WILSON and P. J. E. FORSYTH, *J. Inst. Metals* **94** (1996) 8.
7. I. N. A. OGUOCHA, S. YANNACOPOULOS and Y. JIN, *J. Mater. Sci.* **31** (1996) 5615.
8. D. L. ZHANG and B. CANTOR, in Proceedings of the 2nd Europen Conference on Advanced Materials and Processes, edited by T. W. Cline and P. J. Withers (1991) p. 197.
9. R. P. UNDERHILL, P. S. GRANT and B. CANTOR, *Mater. Design* **14** (1993) 45.
10. H. JONES, *Mater. Sci. Eng.* **5** (1969) 1.
11. M. YAN, W. Z. ZHU and B. CANTOR, *Mater. Sci. & Eng.* A **284** (2000) 77.
12. W. T. KIM, B. CANTOR and T. H. KIM, *Inter. J. Rapid Solidification* **5** (1990) 251.
13. B. CANTOR, *Micron*. **25** (1994) 551.
14. "Metals Handbook, Metallography, Structures and Phase Diagrams," Vol. 8, 8th ed. (ASM, USA, 1973).

Received 8 August 2001
and accepted 27 February 2002